

Colour jumps across the spiral arms of Hubble Ultra Deep Field galaxies

Eric E. Martínez-García,^{1*} Rosa A. González-Lópezlira,², and Ivânia Puerari.³

¹*CONAHCYT Research Fellow - Instituto Nacional de Astrofísica, Óptica y Electrónica, Luis E. Erro 1, Tonantzintla, Puebla, C.P. 72840, México*

²*Instituto de Radioastronomía y Astrofísica, UNAM, Campus Morelia, Michoacán, México, C.P. 58089*

³*Instituto Nacional de Astrofísica, Óptica y Electrónica, Luis E. Erro 1, Tonantzintla, Puebla, C.P. 72840, México*

Accepted XXX. Received YYY; in original form ZZZ

ABSTRACT

We have measured, at various wavelengths, the spiral arm pitch angles of a sample of distant spiral galaxies from the Hubble Space Telescope eXtreme Deep Field (XDF). According to density wave theory, we should detect colour jumps from red-to-blue across the spiral arms. Colour jumps are a consequence of large-scale shocks, which also generate the classic blue-to-red age/colour gradients, and have only been detected until now in nearby spiral galaxies. Our results indicate that colour jumps and gradients have been occurring in distant galaxies for at least the last 8 Gyr, in agreement with density wave theory.

Key words: galaxies: disc – galaxies: general – galaxies: structure – galaxies: kinematics and dynamics – galaxies: star formation – galaxies: high-redshift –

1 INTRODUCTION

The origin of spiral structure in disc galaxies has been a matter of debate over the last decades. The most recent reviews on the topic include those of Dobbs & Baba (2014), Shu (2016), and Sellwood & Masters (2021), who arrive to different conclusions. Dobbs & Baba (2014) argue that the long-lived waves envisioned by density wave (DW) theory (Lin & Shu 1964; Bertin et al. 1989) are not produced in modern numerical simulations, and hence that spiral structure may be only transient and recurrent, as shown by the simulations. On the other hand, Shu (2016) argues in favour of long-lived spirals with a constant spiral pattern speed. DW theory also foretells that large-scale shocks of gas induce star formation (Roberts 1969), and consequently an age (or colour) gradient should be observed across the spiral arms, downstream of the flow for regions inside the corotation radius (R_{CR}),¹ and upstream of the flow for regions outside R_{CR} . There is plenty of observational evidence supporting this scenario (e.g., Gonzalez & Graham 1996; Puerari & Dottori 1997; Egusa, Sofue, & Nakanishi 2004; Tamburro et al. 2008; Egusa et al. 2009; Grosbøl & Dot-

tori 2009; Martínez-García, González-Lópezlira, & Bruzual 2009; Martínez-García, González-Lópezlira, & Gómez 2009; Martínez-García & González-Lópezlira 2011; Sánchez-Gil et al. 2011; Martínez-García & González-Lópezlira 2013; Cerdrés et al. 2013; Martínez-García & Puerari 2014; Yu & Ho 2018; Peterken et al. 2019; Vallée 2021a,b; Karapetyan 2022). Spiral arms also seem to be amplitude-modulated, in accordance with DW theory (Grosbøl 1988; Elmegreen, Elmegreen, & Seiden 1989; Elmegreen 1995; Puerari et al. 2000). Furthermore, Sellwood & Masters (2021) discuss that spiral structure must be primarily a self-excited phenomenon in disc galaxies, and less frequently caused by tidal interactions or bars. Externally excited spiral activity is not long-lived, as expected by DW theory, but instead dissipates in about ten disc rotations (1-2 Gyr; Sellwood & Carlberg 1984, 2014). Spiral arm modes in disc galaxies may be maintained for several rotations if the disc is cooled by gas or other dynamical mechanism that prevents the Toomre parameter from increasing its value, and consequently allows the non-asymmetric structure in the disc to survive. Sellwood & Masters (2021), however, acknowledge that there is no compelling evidence that spiral arms in real galaxies are undoubtedly caused by the mechanisms suggested by numerical simulations (with the exception perhaps of the Milky Way galaxy; see Sellwood et al. 2019).

In this paper we will focus on observations of spiral galaxies beyond our nearby universe, in order to compare

* E-mail: ericmartinez@inaoep.mx

¹ This is the radius where the angular velocity of the density wave, i.e., the pattern speed Ω_p , is equal to the angular velocity of material in the disc, $\Omega(R)$.

them with the predictions of spiral structure formation theories and numerical simulations.

1.1 Colour gradients across spiral arms

There are two opposite but coexisting colour gradients that can be observed across spiral arms (see, e.g., [Yu & Ho 2018](#)). The first one actually envisioned by [Roberts \(1969\)](#), i.e., the ‘classic’ age (colour) gradient, is caused by the aging of newborn stars as they drift away from the spiral arms. For trailing spirals, the expected colour sequence is blue-to-red (see Figure 1, left panel). This is the kind of gradient studied by [Gonzalez & Graham \(1996\)](#) and [Martínez-García, González-Lópezlira, & Bruzual \(2009\)](#), who employ a reddening-free Q -index to trace aging newborn stars. Classic age gradients are difficult to observe along the entire spiral arms due to masking by dust, radiation from HII regions, and the substructure itself of the spiral arms (e.g., [La Vigne, Vogel, & Ostriker 2006](#); [Shetty & Ostriker 2006](#)). Nevertheless, the statistics of ‘classic’ age gradients agree with the theoretical expectations, even when a circular model (i.e., one that neglects non-circular motions) is employed to determine Ω_p (see e.g., [Martínez-García, González-Lópezlira, & Gómez 2009](#); [Martínez-García & González-Lópezlira 2015](#)).

The other ‘gradient’ that can be detected across spiral arms is a ‘colour jump’ from red-to-blue (see Figure 1, right panel). [Gittins & Clarke \(2004\)](#) predicted that the pitch angle² of the star-formation (SF-) arm, P_{SF} (traced by newly born stars), should be smaller than the pitch angle of the potential minimum (or local maximum surface mass density, P -arm), P_{pot} (traced by old stars, i.e., the density wave), such that $P_{SF} < P_{pot}$. In this scenario, spiral arms at shorter wavelengths are expected to have a smaller pitch angle (more tightly wound arms). The colour jump is due to the angular offset between the P -arm and the SF-arm, which is proportional to the difference between the angular velocity of the stars and gas in the disc, and the pattern speed, $\Omega - \Omega_p$. Because this difference vanishes at corotation, the angular offset between the two arms will also vanish, which requires $P_{SF} < P_{pot}$. On the other hand, the shock (traced by the dust lanes and with the maximum gas density), upstream of the P -arm, is expected to have a pitch angle, P_{shock} , equal to or smaller than P_{pot} , but larger than P_{SF} ([Gittins & Clarke 2004](#)). Colour jumps have been successfully detected by [Grosbøl & Patsis \(1998\)](#), [Martínez-García & González-Lópezlira \(2013\)](#), [Martínez-García et al. \(2014\)](#), [Yu & Ho \(2018\)](#), and [Lin et al. \(2022\)](#).

If density waves were already triggering star formation several Gyr ago, we should be able to observe ‘colour jumps’ across spiral arms in galaxies with redshifts $z > 0.1$. Other compelling theories, such as self-propagating star formation ([Mueller & Arnett 1976](#); [Gerola & Seiden 1978](#)), or transient and recurrent arms ([Grand, Kawata, & Cropper 2013](#); [Michikoshi & Kokubo 2014](#)), where the spiral arm pitch angle is mainly constrained by the shear rate of the

² The angle between a tangent to the spiral arm at a certain point and a circle, whose centre coincides with the galaxy’s, that crosses the same point.

Table 1. PSF FWHM of the XDF data, obtained by measuring foreground stars in the 60 mas images.

Filter	FWHM (")
F435W	0.107
F606W	0.111
F775W	0.107
F814W	0.118
F850LP	0.108
F105W	0.181
F125W	0.179
F140W	0.181
F160W	0.184

galactic rotation curve, do not predict any colour jumps or age (colour) gradients.

This paper is organized as follows. In Section 2 we present the galaxy sample, in Section 3 we delineate the analysis, in Section 4 we describe and discuss the results, and finally in Section 5 we give our conclusions.

2 GALAXY SAMPLE

The selection of our sample of galaxies was first made by inspecting the data products of the *Hubble Space Telescope (HST)* eXtreme Deep Field (XDF, [Illingworth et al. 2013](#)). The XDF combines data sets from the original Hubble Ultra-Deep Field (HUDF, [Beckwith et al. 2006](#)), the HUDF09, the Cosmic Assembly Near-infrared Deep Extragalactic Legacy Survey (CANDELS, [Grogin et al. 2011](#)), the HUDF12, and supernovae follow-ups. There are two data sets with a pixel scale of 30 milliarcseconds (mas), and 60 mas, respectively. The 30 mas data set comprises five optical filters: F435W, F606W, F775W, F814W, and F850LP, from the Advanced Camera for Surveys (ACS), while the 60 mas data set includes the aforementioned optical ACS filters plus four Wide-Field Camera 3 (WFC3) near-infrared (NIR) filters: F105W, F125W, F140W, and F160W. The *HST* point-spread function (PSF) full-width-at-half-maximum (FWHM) is $\sim 0.^{\prime\prime}1 - 0.^{\prime\prime}2$ (see Table 1).

We combined the 30 mas images into a single frame (thus maximizing the signal-to-noise ratio, S/N). Next, we split the image into $12'' \times 12''$ boxes covering the entire image, which measures approximately $\sim 200'' \times 200''$. We focused on selecting grand design, non-barred (SA) or weakly barred (SAB) spiral galaxies.³ The initial candidate sample consisted of 23 objects (see Figure 2). We verified that each candidate has a rotating disc. To achieve this goal we used data from the Multi-Unit Spectroscopic Explorer (MUSE, [Bacon et al. 2010](#)) integral-field spectrograph on the Very Large Telescope (VLT). We retrieved from the European

³ Spirals arms in barred galaxies (SB) may have an origin other than density waves, e.g., chaotic orbits guided by invariant ‘manifolds’ (see, e.g., [Romero-Gómez et al. 2006](#); [Patsis 2006](#); [Martínez-García 2012](#); [Athanasoula 2012](#); [Contopoulos 2022](#)). This theory also predicts a constant spiral pattern speed, although with lifetimes shorter than those anticipated by density wave theory.

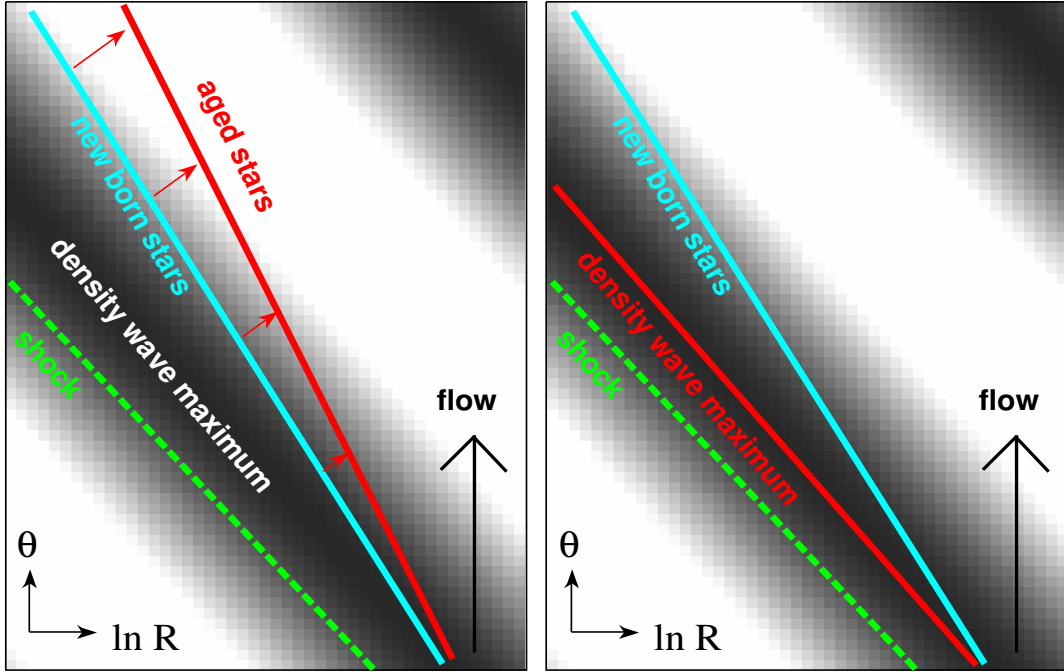


Figure 1. Left panel: Classic age gradient across trailing spiral arms (blue-to-red), in the $\ln R$ vs. θ plane, for radii $R < R_{CR}$. The spiral shock, density wave, newborn stars, and aged stars are represented by the dashed green line, dark gray region, continuous blue line, and continuous red line, respectively. Right panel: Colour jump across trailing spiral arms (red-to-blue). The spiral shock, density wave maximum, and new born stars, are represented by the dashed green line, continuous red line, and continuous blue line, respectively. The ‘colour jump’ is located upstream of the classic age gradient (see left panel). In this plot, a circle ($R=\text{constant}$) is represented by a vertical line and has a pitch angle of $P = 0^\circ$.

Southern Observatory (ESO) Science Archive data belonging to the MUSE Hubble Ultra Deep Survey (HUDF; Bacon et al. 2017), and the MUSE Extremely Deep Field (Bacon et al. 2021). The MUSE HUDF data cubes have a spatial sampling (pixel scale) of $\sim 0''.2$, and a spectral sampling of 1.25 \AA over the wavelength range $4750 \text{ \AA} - 9350 \text{ \AA}$. The PSF FWHM of the MUSE data is $\sim 0''.71$ at 4750 \AA , and $\sim 0''.57$ at 9350 \AA , owing to the ESO adaptive optics methods. We identified each one of our objects in the MUSE cubes, subtracted the local sky, and obtained moment-1 (velocity) maps by using:

$$v = c \left(\frac{\int_{\lambda_0}^{\lambda_1} \lambda I_\lambda d\lambda}{(1+z)\lambda_{\text{rest}} \int_{\lambda_0}^{\lambda_1} I_\lambda d\lambda} - 1 \right), \quad (1)$$

where v is the observed velocity, c is the speed of light, λ is the observed wavelength, I_λ is the intensity at wavelength λ , $\lambda_0 - \lambda_1$ is the observed wavelength range of a certain emission line, z is the redshift of the galaxy, and λ_{rest} is the rest wavelength of the emission line. The brightest emission lines for various HUDF objects are given in Inami et al. (2017). For this work we use emission lines devoid of residual sky lines. Depending on the object, the adopted emission lines were one among [O II] $\lambda 3726$, [O II] $\lambda 3729$,⁴ H β , and H α . In Figure 3 we show the spectrum near the H α line used to derive

the moment-1 map of UDF 3822. Similar spectra were obtained for most of the objects in our sample. From this analysis we were able to confirm disc rotation in 16 galaxies. There are no data for UDF 295 in the MUSE HUDF. For the rest of the objects the spatial resolution of the MUSE cubes is poor, hence we could not confirm or disprove disc rotation. These objects are UDF 295, UDF 3257, UDF 3680, UDF 4225, UDF 6188, UDF 7315, and UDF 7432. We retrieved data for them from the Atacama Large Millimeter/submillimeter Array (ALMA) Science Archive.⁵ Unfortunately, we likewise could not find evidence of disc rotation, due to either a synthesised beam larger than the angular size of the objects, or to lack of bright emission lines. We exclude these galaxies from further analysis.

Our final sample consists of 16 objects that are listed in Table 2. Moment-1 maps are shown in Figure 4. Spec-

⁴ The [O II] 3726 - 3729 \AA doublet was treated as two separate lines.

⁵ Project codes: ADS/JAO.ALMA#2012.1.00173.S, ADS/JAO.ALMA#2015.1.00098.S, ADS/JAO.ALMA#2015.1.00543.S, ADS/JAO.ALMA#2016.1.00324.L, and ADS/JAO.ALMA#2017.1.00138.S. ALMA is a partnership of ESO (representing its member states), NSF (USA) and NINS (Japan), together with NRC (Canada), MOST and ASIAA (Taiwan), and KASI (Republic of Korea), in cooperation with the Republic of Chile. The Joint ALMA Observatory is operated by ESO, AUI/NRAO and NAOJ. The National Radio Astronomy Observatory is a facility of the National Science Foundation operated under cooperative agreement by Associated Universities, Inc.

troscopic redshifts were taken from Inami et al. (2017); a histogram of the redshift distribution is shown in Figure 5. Also in Table 2, we list in column 6 the spectral energy distribution (SED) templates fitted to obtain the photometric redshift of each object, as described in Rafelski et al. (2015, ; see also Benítez (2000), Coe et al. (2006)). A histogram of the template types is shown in Figure 6. The SED templates include spiral galaxies, with Hubble types Sbc and Scd (template numbers 6 and 7, respectively); starburst galaxies (SB, template numbers 8–11); and lenticular galaxies (template number 5). Templates with intermediate numbers are created by interpolation. The best fit SED template may imply a preliminary galaxy type classification.

We also corroborate that our objects have active star formation in their discs. For this purpose we use the Code Investigating GALaxy Emission (CIGALE, Burgarella et al. 2005; Noll et al. 2009; Boquien et al. 2019); we employ the aperture photometry measurements of Rafelski et al. (2015), and include the ultra-violet filters when available. The instantaneous star formation rate (SFR), Ψ , is given in Table 3,⁶ together with the average SFR over the last 10 Myr, $\langle \Psi \rangle^{10 \text{ Myr}}$, and the average SFR over the last 100 Myr, $\langle \Psi \rangle^{100 \text{ Myr}}$. All of our objects are actively forming stars, i.e., they have an SFR, $\Psi > 1 \text{ M}_\odot \text{ yr}^{-1}$.

3 ANALYSIS

For the sample galaxies we obtain the projection parameters, i.e., the inclination and position angles (I.A and P.A., respectively, see Table 4), by fitting ellipses to their outer isophotes in the combined 30 mas images. After deprojecting the images, we proceeded to measure the pitch angles, P , of the spiral arms in each individual 30 and 60 mas image, by way of Fourier transform techniques. We first transform the images from Cartesian (x, y) to logarithmic polar coordinates $\ln R, \theta$; $\ln R \equiv u$; we then compute the two-dimensional Fourier transform (e.g., Puerari & Dottori 1992; Saraiva Schroeder et al. 1994):

$$A(m, p) = \frac{\int_{u_{\min}}^{u_{\max}} \int_{-\pi}^{\pi} I(u, \theta) e^{-i(m\theta + pu)} d\theta du}{\int_{u_{\min}}^{u_{\max}} \int_{-\pi}^{\pi} I(u, \theta) d\theta du}, \quad (2)$$

where $I(u, \theta)$ is the radiation intensity of the pixel with coordinates (u, θ) . The values u_{\min}, u_{\max} delimit the radial region of the spiral arms given by $\Delta R = (R_{\min} - R_{\max})$. In order to avoid potential biases we use the same ΔR at all wavelengths/passbands for the same object (see also Yu & Ho 2018). The adopted ΔR values are given in Table 4 in units of arcseconds and in kpc (taking into account cosmological effects, Wright 2006; Bennett et al. 2014); they were chosen by visually inspecting the images in order to include the spiral arms and avoid the central bulge. The cosmological surface brightness dimming, $\sim (1+z)^{-4}$, may affect our P measurements, in the sense that higher-redshift galaxies may be measurable only in their inner regions. This affects mostly diffuse, rather than compact, objects (e.g., Calvi et

⁶ See Appendix A for the input configuration adopted in CIGALE.

al. 2014). However, even if the cosmological surface brightness dimming affects the observed spiral loci of our galaxies, any differences of P with wavelength will still be detected.

From the output $A(m, p)$ matrix we derive the pitch angle with:

$$\tan P = -m/p_{\max}, \quad (3)$$

where $m = 0, 1, 2, 3 \dots$ All our objects have a bisymmetric spiral, hence we adopt $m = 2$ for all the calculations. The values of p_{\max} at each wavelength and for each object are found by computing the absolute maximum of the $A(m = 2, p)$ spectra. In Figure 7 we show the $A(m = 2, p)$ spectra for UDF 7556, at different wavelengths.

Star-forming clumps are less abundant in nearby galaxies than at higher redshifts (e.g., Adams et al. 2022; Sattari et al. 2023). Since these clumps are assumed to be related to star formation, no masks were applied to them. Also, the Fourier transform technique described above separates the signals of the different components contributing to the luminosity in the image. For this reason, the P measurements are not expected to show significant differences in the presence of massive star-forming clumps, unless their presence effectively suppresses the signal from the spiral arms. This is not the case for the galaxies in our sample (see Figure 2).

3.1 The effect of angular size for distant galaxies

In this section we explore the effect that angular size has on our measurements of pitch angles for disc galaxies at redshifts $z > 0$ (see also Block et al. 2001). For this purpose we simulate the appearance of the grand design spiral galaxy M51 (NGC 5194) at different redshifts. We use the *HST* F814W-band mosaic of M51 obtained from the Hubble Legacy Archive. This image was secured with the ACS WFC, whose pixels are $0''.05$ on the side. We assume a distance of 8.58 ± 0.10 Mpc ($z \sim 0$, McQuinn et al. 2016), an inclination angle of 20° , and a position angle of 172° (Leroy et al. 2008). At the assumed distance of M51, $0''.05$ is ~ 2 pc. We use the cosmological calculator of Wright (2006) to derive the angular size of M51 at different redshifts. The results of this simulation, at fixed pixel scale, are shown in Figure 8. At $z \sim 0$, the pitch angle is $P \sim 19^\circ$ (Puerari, Elmegreen, & Block 2014). At redshift $z \sim 2$, one ACS WFC pixel is ~ 400 pc, the observed wavelength is $\lambda_{\text{obs}} \sim 2.4 \mu\text{m}$ and the mean P value increases to $P \sim 22^\circ$, with a larger 1σ error. For redshifts higher than $z \gtrsim 2$, the P value decreases again due to the standard cosmological model, which predicts an angular diameter turnover point (e.g., Melia & Yennapureddy 2018).⁷ The higher P values at intermediate redshifts are due to the ‘pixellation’ of the spiral arms: as we increase the redshift of M51, and keep the pixel scale fixed, fewer pixels trace the spiral arms in the image. In Figure 9 we show the M51 image at redshift $z = 0$ (left frame) and at $z = 1.9$ (right frame). The simulated $z = 1.9$ galaxy is ~ 200 times smaller in angular size and hence encompasses many fewer pixels. From this exercise we can conclude that the pitch angles for galaxies at $0 < z < 2$ may suffer from ‘pixellation’,

⁷ This is a cosmological effect in the apparent angular diameter due to the expansion of the universe and the finite speed of light.

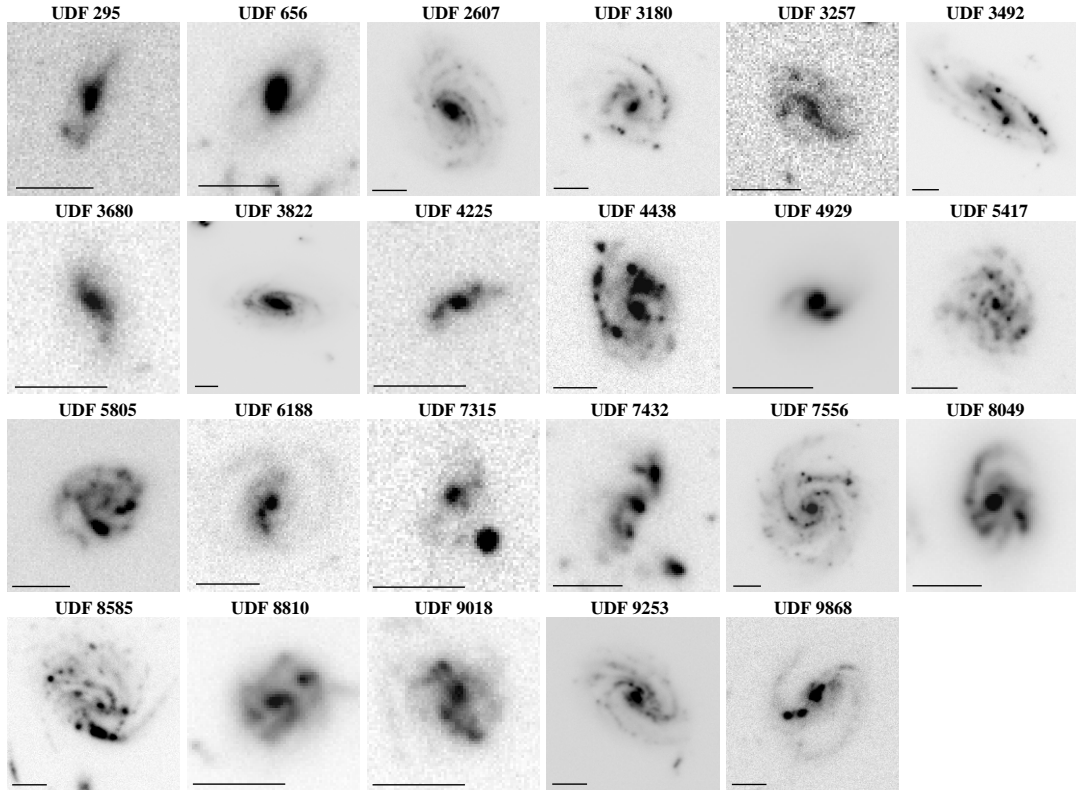


Figure 2. Combined 30 mas images of spiral galaxy candidates. The horizontal line in the lower left corner of each frame represents 1''. The display is in linear scale. North is up, east to the left.

Table 2. Spiral galaxy sample.

UDF-ID (Coe et al. 2006)	R.A. (J2000, deg) (this work)	Decl. (J2000, deg) (this work)	UVUDF-ID (Rafelski et al. 2015)	Spectroscopic redshift z (Inami et al. 2017)	SED Template (Rafelski et al. 2015)
656	53.164455	-27.815337	830	1.096718	6.2
2607	53.180240	-27.798929	21364	0.667092	6.2
3180	53.157823	-27.797522	3103	0.767559	8.5
3492	53.187823	-27.794047	51705	0.345790	8.5
3822	53.186947	-27.790995	22719	0.213732	6.6
4438	53.137642	-27.791988	52744	0.997884	7.8
4929	53.187952	-27.789999	22718	0.435454	6.3
5417	53.166166	-27.787515	22410	1.095512	7.3
5805	53.192043	-27.787163	34879	1.095373	7.9
7556	53.169922	-27.771048	24587	0.622005	6.9
8049	53.162345	-27.775059	24348	0.419313	7.3
8585	53.147860	-27.774034	54454	1.087423	7.9
8810	53.155280	-27.769540	24453	0.736333	7.7
9018	53.147061	-27.778419	9759	1.086319	9.2
9253	53.178387	-27.768230	24420	0.668620	6.7
9868	53.163590	-27.758934	37143	1.094886	5.7

and result in artificially higher pitch angles and errors. These effect is more deleterious for images with coarser plate scales. For instance, if we use the Sloan Digital Sky Survey (SDSS) i -band mosaic of M51 (plate scale = $0.^{\prime\prime}396 \text{ pixel}^{-1}$, Ahn et al. 2014; Alam et al. 2015), we find that the pitch angle increases by a factor of ~ 1.5 times, and the 1σ error grows

by a factor of ~ 6 in the redshift range $0 < z < 0.16$.⁸ It is important to mention that this effect affects the P measurements at every λ in a similar manner. That being said, at a fixed redshift, the difference in the measured pitch angles at

⁸ For $z \gtrsim 0.16$, the spiral arms of M51 are no longer distinguishable for images with the same pixel scale as the SDSS mosaic.

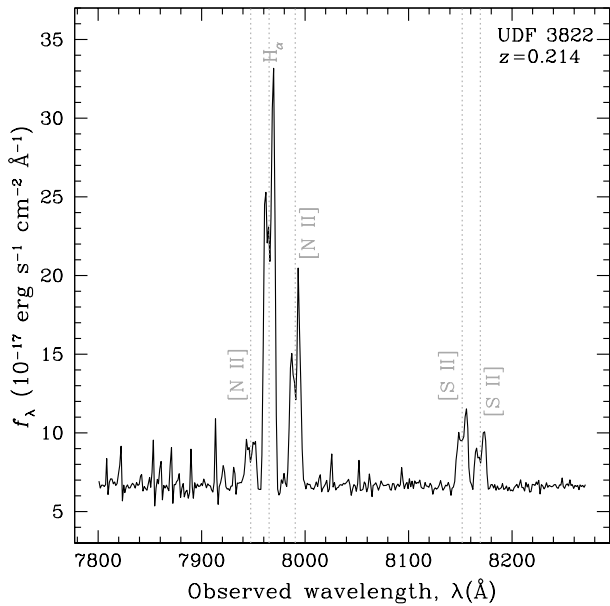


Figure 3. Zoom-in on the MUSE spectrum of the galaxy UDF 3822, integrated over all spatial pixels. Some emission lines are labelled.

Table 3. Star formation rates, Ψ .

UDF-ID	Ψ ($M_\odot \text{ yr}^{-1}$)	$\langle \Psi \rangle^{10 \text{ Myr}}$ ($M_\odot \text{ yr}^{-1}$)	$\langle \Psi \rangle^{100 \text{ Myr}}$ ($M_\odot \text{ yr}^{-1}$)
656	7.5 ± 3.0	7.5 ± 3.1	7.9 ± 4.1
2607	19.7 ± 15.6	20.1 ± 16.4	27.1 ± 32.0
3180	4.5 ± 0.2	4.8 ± 0.2	9.6 ± 0.5
3492	2.9 ± 1.7	3.0 ± 1.8	6.1 ± 3.3
3822	7.2 ± 6.6	7.5 ± 7.0	13.1 ± 14.6
4438	10.6 ± 1.8	11.1 ± 1.8	20.2 ± 2.4
4929	4.5 ± 1.0	4.5 ± 1.0	4.6 ± 1.0
5417	21.8 ± 7.8	22.2 ± 7.8	28.8 ± 10.8
5805	7.6 ± 2.9	7.9 ± 3.0	13.7 ± 5.2
7556	16.7 ± 4.5	16.9 ± 4.4	19.8 ± 5.0
8049	3.6 ± 0.9	3.8 ± 0.9	6.6 ± 1.5
8585	32.1 ± 5.7	33.6 ± 5.7	60.4 ± 6.7
8810	4.2 ± 0.9	4.4 ± 0.9	7.8 ± 1.3
9018	3.7 ± 0.2	3.9 ± 0.2	7.8 ± 0.4
9253	16.1 ± 4.2	16.2 ± 4.2	17.8 ± 4.8
9868	17.5 ± 15.9	17.6 ± 15.9	18.3 ± 16.8

different wavelengths will still be detected if present in real galaxies.

3.2 Differences in the PSF.

For distant objects, which are imaged by considerably fewer pixels than nearby objects, a difference in the PSF for different filters may produce faulty pitch angle measurements. In the case of the 30 mas XDF data, the PSF FWHM is practically the same at all wavelengths ($\sim 0\farcs1$, Windhorst et al. 2011), and no corrections are needed. This is not the case for the 60 mas data (see Table 1), where the four NIR

images have a PSF FWHM ~ 1.6 times larger than the optical images. In order to test the impact of a different PSF on the observations of distant spiral galaxies, we use the simulated M51 image at redshift $z \sim 1.4$, produced in Section 3.1 from the Hubble Legacy data. We convolve this image with a Gaussian kernel with different values of σ . The result of this exercise is displayed in Figure 10. As shown in the plot, a larger FWHM results in a higher P value. This effect may bias our measurements of the pitch angles. With the purpose of minimising this effect on the 60 mas data, and since we are interested in pitch angle relative differences, rather than in their absolute values, we correct the optical images (filters F435W, F606W, F775W, F814W, and F850LP) to match the NIR PSF FWHM (filters F105W, F125W, F140W, and F160W). We assume that the PSF matching can be achieved through a convolution with a Gaussian kernel (see also Aniano et al. 2011), i.e., we posit that the output PSF FWHM is the result of the convolution of two Gaussian functions, $\sigma_{f*g} = \sqrt{\sigma_f^2 + \sigma_g^2}$, where σ_f and σ_g are the standard deviations of the two original Gaussians, and the result of the convolution is also Gaussian. The 60 mas data were corrected before analysis.

We also tested the effect of a different PSF on the nearby galaxy M51 by using far and near ultraviolet (FUV and NUV, respectively) imaging from the GALEX Ultraviolet Atlas of Nearby Galaxies (Gil de Paz et al. 2007), and u -, g -, r -, i - and z -band optical data from SDSS (Ahn et al. 2014; Alam et al. 2015). We registered the SDSS images to the spatial resolution of the NUV image (which has a plate scale of $1.5'' \text{ pixel}^{-1}$). The GALEX images have a PSF with a FWHM a factor of ~ 4 larger than SDSS frames. In order to get a common PSF for all our data, we use the 2017 version of the convolution kernels of Aniano et al. (2011). We found that the pitch angles obtained from the PSF-corrected optical images are slightly higher ($\sim 0.4^\circ$) than the ones without it; however, this difference is similar to the computation error of the method. Hence, we can conclude that, for nearby galaxies, a different PSF does not produce, in practice, a variation on the pitch angle measurements.

4 RESULTS AND DISCUSSION

The results of the measured pitch angles for the 30 mas data are given in Table 4 and plotted in Figure 11 as a function of rest wavelength $\lambda_{\text{rest}}(\text{\AA})$. In this work we use the following convention: the objects with an ‘S’ on-the-sky view have positive pitch angles (P), and the objects with a ‘Z’ on-the-sky view have negative P values (see equation 3). No P value is accepted when its sign does not agree with the ‘S’ or ‘Z’ on-the-sky view. Similarly, the results for the 60 mas data are given in Table 5 and Figure 12.

In order to quantify the correlation of P with λ_{rest} , we fit a linear relation $P(\lambda_{\text{rest}}) = a + b\lambda_{\text{rest}}$ to the values of the pitch angles obtained from the NIR filters (see also Section 4.2) for each object, individually. The results are given in Table 6, where r_{xy} is the correlation coefficient (Bevington 1969), and $\Delta\lambda_{\text{rest}}$ indicates the wavelength range at rest for which the pitch angles are measured. From these fits we can determine if $|P|$ (the absolute value of the pitch angle) decreases for shorter wavelengths, as expected for the

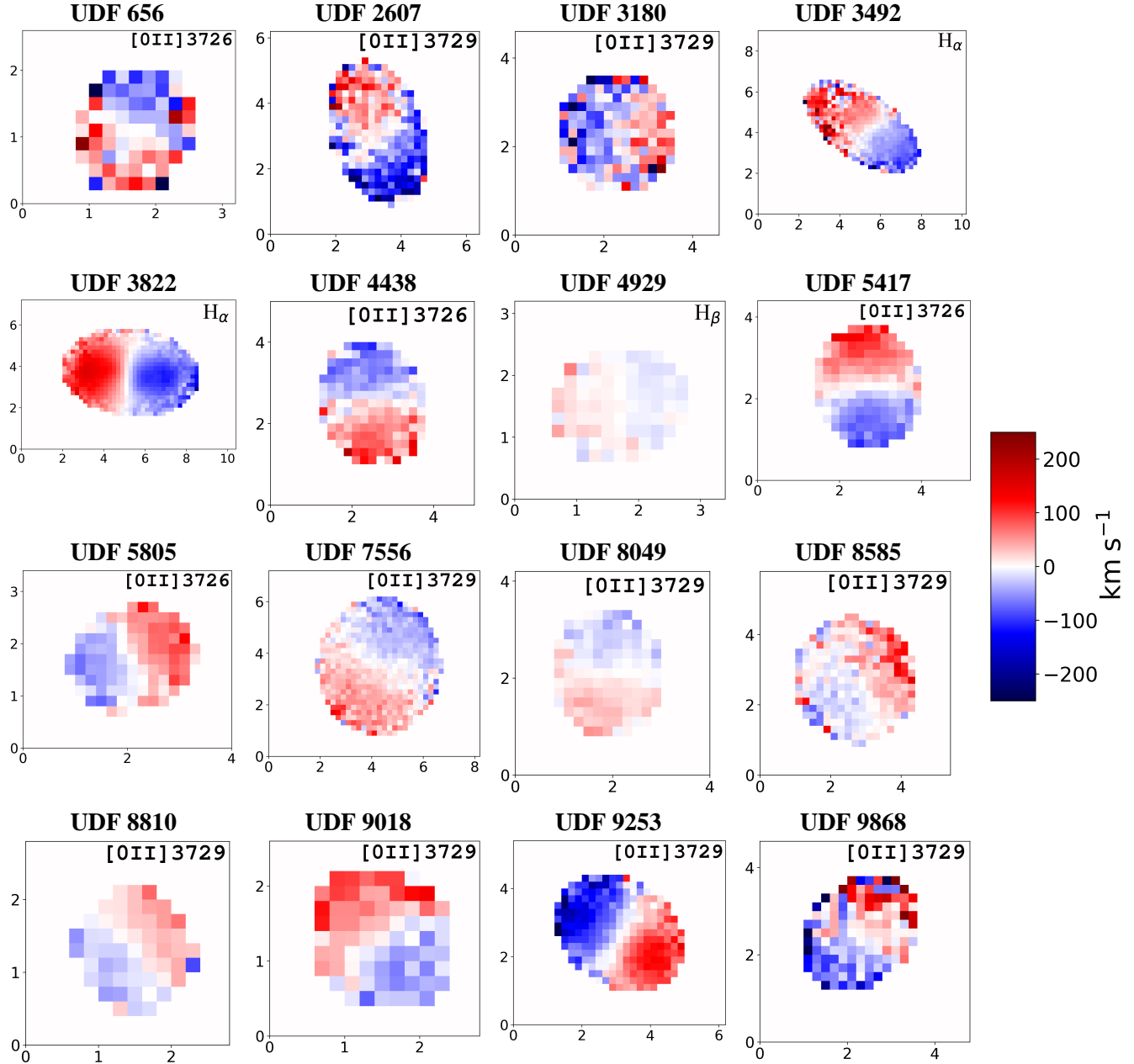


Figure 4. Moment-1 (velocity) maps of the galaxy sample (see Table 2). Axis units are in arcseconds ('').

colour jumps (see Section 1.1) of trailing spiral arms. For most of the objects we find the expected colour jump trend, i.e., the absolute value of the pitch angle $|P|$ decreases for shorter wavelengths. However, for three objects, UDF 4929, UDF 8585, and UDF 9253, we find the opposite, i.e., the $|P|$ value increases for shorter wavelengths. In Table 6 we have catalogued the colour jumps for these objects as ‘reverse’, i.e., from blue-to-red, as opposed to ‘normal’, i.e., from red-to-blue. Interestingly, the three ‘reverse’ colour jump galaxies have a ‘Z’ on-the-sky view, but the effect is important only for UDF 9253. In the cases of UDF 4929 and UDF 8585, the pitch angles are almost constant with wavelength.

4.1 Leading spiral arms?

At $z \approx 0$ there are practically no leading galaxies, i.e., with the tails of the spiral arms pointing in the direction of galactic rotation, among the thousands known (e.g., Väistönen et al. 2008; Grouchy et al. 2008; Lieb, Collier, & Madigan 2022). We may test whether the arms of our three ‘reverse’ colour jump galaxies are indeed leading, using the position of the dust lanes. For regions inside R_{CR} , grand design spirals often have dust lanes along the inner edge (or the concave side) of the arms (Grosbøl, Block, & Patsis 1999). Unfortunately, dust lanes are not detected in UDF 4929 and

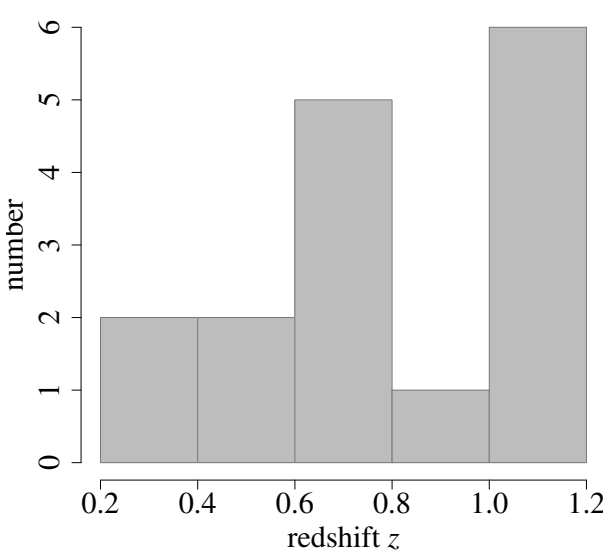


Figure 5. Histogram of the spectroscopic redshifts of our galaxy sample.

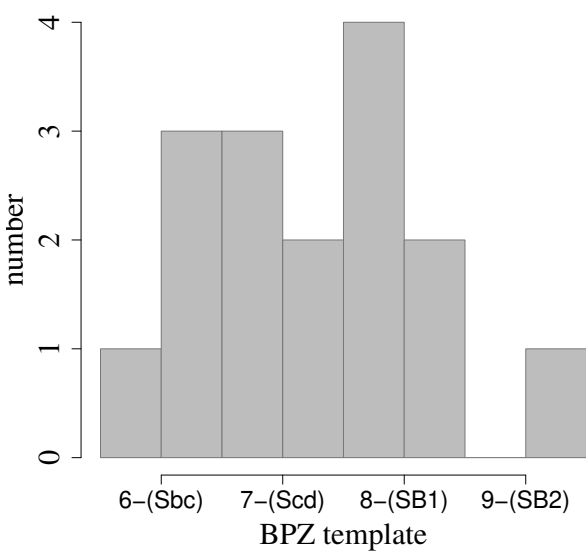


Figure 6. Histogram of SED templates fitted to the sample (Rafelski et al. 2015). Spirals are designated Sbc and Scd (template numbers 6 and 7), and starbursts are designated SB1 and SB2 (template numbers 8 and 9).

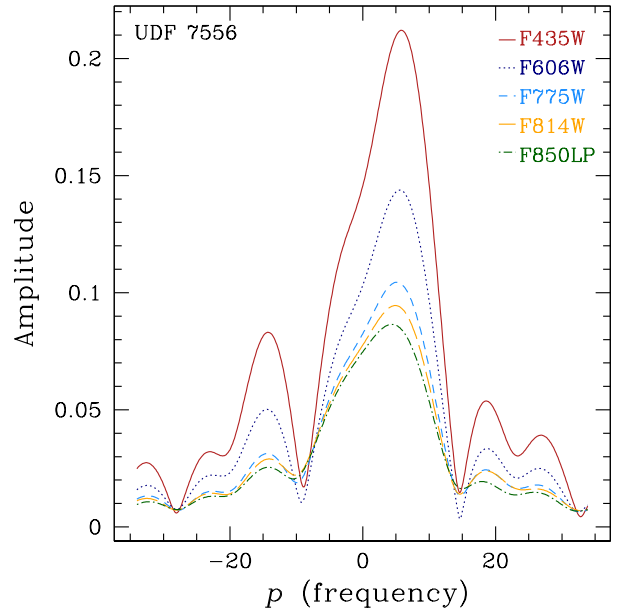


Figure 7. $A(m = 2, p)$ spectra for UDF 7556, computed for the 30 mas images in filters F435W, F606W, F775W, F814W, and F850LP. The maximum amplitude determines the value of p_{\max} for each filter (see equation 3).

UDF 8585, and are just barely discerned in UDF 9253, due to the limited spatial resolution. We can also employ the method of Väisänen et al. (2008) to determine if a galaxy is rotating clockwise or counterclockwise. This procedure relies on the assumption that the side of a disc galaxy closer to the observer shows more dust extinction. The sense of rotation can be inferred from the rotation curve. To implement this method we measured the surface brightness profiles along the minor axis of the discs in our galaxy sample. The results of this analysis are not convincing, since we obtained nearly the same number of leading and trailing spirals. This may indicate that the method is effective only for certain, but not all, relative spatial distributions of dust and stars in galactic discs. A colour asymmetry in the discs may also suggest which side is near or far from the observer. In Martínez-García, González-Lópezlira, & Bruzual (2009), we found that in $\sim 50\%$ of a sample of 31 face-on spiral galaxies of various Hubble types, the photometric Q -index [$Q(rJgi) = (r - J) - \frac{E(r - J)}{E(g - i)}(g - i)$] shows two average values, one for each half of the image. We dubbed these ‘ Q effect’ galaxies. For this small sample it is not clear whether the disks are divided along their projected mayor axes or not. Although the ‘ Q effect’ may suggest near/far disc sides, not all the objects show it, which suggests that the dust and stars relative distributions are not the same for all galaxies. The ‘ Q effect’ may be a consequence of a reflection in the disc resulting in artificial asymmetries [see the case of NGC 3521 in Zibetti, Charlot, & Rix (2009)]. A proposed correlation between dust attenuation and galaxy mass (Lorenz et al. 2023) may also affect this behaviour. Having said that, any conclusion derived from colour asymmetries (even with UV

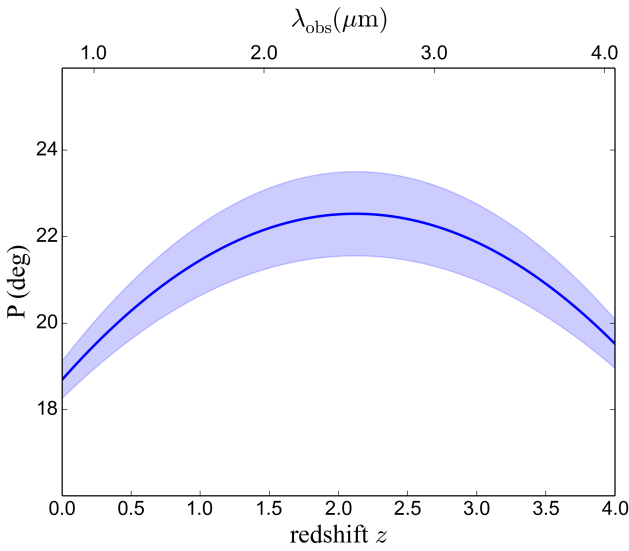


Figure 8. Pitch angles of M51 (NGC 5194), as a function of simulated redshift z . The $z = 0$ data corresponds to the *HST* F814W image. Solid blue line: mean value; shaded region: $\pm 1\sigma$ error. The upper x axis denotes the observed wavelength, $\lambda_{\text{obs}} = \lambda_{\text{rest}}(1+z)$.

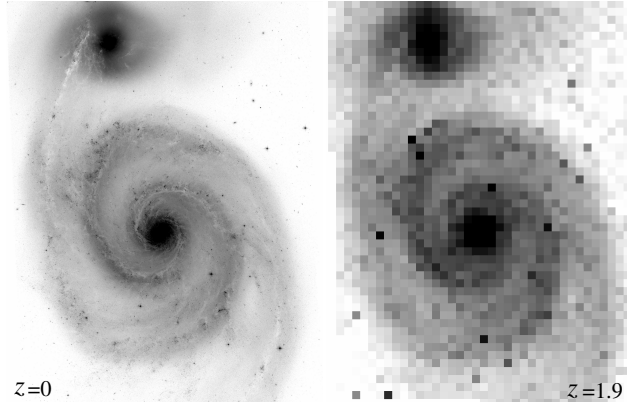


Figure 9. Left: Mosaic of the spiral galaxy M51 in the *HST* F814W filter at redshift $z = 0$. Right: Simulated image of M51 at redshift $z = 1.9$, $\lambda_{\text{obs}} \sim 2.4\mu\text{m}$, obtained by assuming the same pixel scale as the F814W image.

filters) would require further analysis outside the scope of this work.

According to theoretical frameworks, the leading appearance of the spiral arms may be explained if they are undergoing the leading phase of the swing amplification (e.g., Goldreich & Tremaine 1978; Toomre 1981) or the WASER (Mark 1976) mechanism. In these frameworks, the spiral arms are expected to originate as leading waves, evolve to amplified trailing waves, and eventually fade out. In modern numerical simulations, ‘swing amplified’ spirals can be explained as the superposition of a few long-lived patterns (see, e.g., Valencia-Enríquez, Puerari, & Chaves-Velasquez 2017; Sellwood & Carlberg 2021). In Figure 13

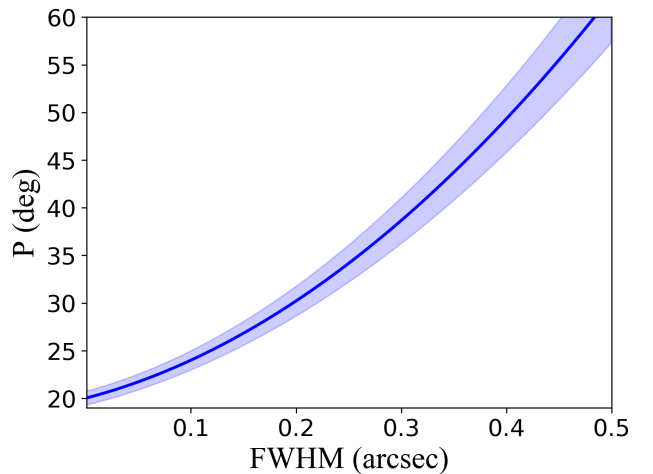


Figure 10. Pitch angles of the simulated M51 image, at redshift $z = 1.4$, after convolving the image with Gaussian kernels with different FWHMs (i.e., different PSF).

we show a contour plot of two uniformly-rotating spiral patterns. If we assume that the inner spiral (red contours) rotates with a higher Ω_p , than the outer spiral (blue contours), and use Equation 2 to compute the $A(m = 2, p)$ spectra as a function of time, we obtain the plot in Figure 14. From this graph it is evident that the global pattern (resulting from the superposition of the two spiral patterns in Figure 13) has a recurring cycle that shifts from leading ($p < 0$) to trailing ($p > 0$). In order for this outcome to explain the apparently ‘leading’ spiral arms that we observe with the colour jumps it would be necessary for the gas to adjust rapidly to the changes in the spiral potential (see, e.g., Sellwood & Masters 2021). Also, the amplitude of the ‘leading’ phase of the spiral pattern should be higher than the amplitude of the ‘trailing’ phase at a given time. However, as shown in Figure 14, the amplitude of the ‘trailing’ phase always dominates the $A(m, p)$ spectra and, consequently, it would be difficult to actually observe the ‘leading’ phase. The presence of ‘hidden’ leading patterns can be indirectly inferred from the modulation of the spiral arms (e.g., Elmegreen, Elmegreen, & Seiden 1989; Puerari et al. 2000). These patterns will not appear directly on the images, but they can create interference signatures on the density contours along the arms. In our case, the apparently ‘leading’ spirals are clearly distinguishable and thus cannot be explained in the context of numerical simulations.

Finding *bona fide* leading spiral arms in galaxies in the distant universe may help to better constrain some theories about the nature of spiral galaxies. For instance, if a statistically significant number of galaxies have leading spiral arms at a certain redshift, there is the possibility that they are ‘swing amplified’ (Toomre 1981). Moreover, if leading arms are indeed due to interactions, we would expect the number of spiral galaxies with leading arms to increase at $z = 2$ and beyond, just as quasars (also attributed to interactions) have their golden age between $z = 2$ and $z = 3$ (e.g., Shaver et al. 1996). At larger redshifts, the black holes may not have had enough time to become massive. Leading arms would

only require interactions, whose number seem to diminish continuously between $z = 2$ and $z = 0$. However, the question would still remain about how leading spiral arms could survive long enough to be observed as density waves.

Table 4. Analysis parameters and measured pitch angles (P) for the 30 mas data.

UDF-ID	I.A. (°)	P.A. (°)	ΔR	F435W (°)	F606W (°)	F775W (°)	F814W (°)	F850LP (°)
656	52.3	139.3	(0.36-0''.90) (2.98-7.46 kpc)	-28.4 (± 0.9)	-25.4 (± 0.7)	-24.7 (± 0.7)	-24.7 (± 0.7)	-32.3 (± 1.1)
2607	44.1	20.0	(0.78-1''.20) (5.53-8.51 kpc)	--	35.3 (± 1.3)	39.6 (± 1.6)	36.6 (± 1.4)	41.2 (± 1.7)
3180	21.3	159.4	(0.48-1''.20) (3.60-8.99 kpc)	--	--	-26.6 (± 0.8)	-26.6 (± 0.8)	-27.4 (± 0.8)
3492	68.6	55.3	(1.32-2''.28) (6.53-11.28 kpc)	17.7 (± 0.3)	15.7 (± 0.3)	14.7 (± 0.2)	15.2 (± 0.2)	15.4 (± 0.3)
3822	58.1	83.5	(0.60-1''.53) (2.10-5.36 kpc)	14.7 (± 0.2)	16.2 (± 0.3)	17.5 (± 0.3)	18.5 (± 0.4)	20.6 (± 0.5)
4438	43.2	20.0	(0.30-1''.50) (2.44-12.18 kpc)	28.9 (± 0.9)	31.8 (± 1.1)	32.9 (± 1.1)	34.1 (± 1.2)	34.1 (± 1.2)
4929	40.2	108.9	(0.36-1''.02) (2.05-5.82 kpc)	--	-22.9 (± 0.6)	-22.9 (± 0.6)	-21.2 (± 0.5)	-20.7 (± 0.5)
5417	33.4	8.7	(0.24-0''.78) (1.99-6.46 kpc)	--	-21.1 (± 0.5)	-21.1 (± 0.5)	-21.1 (± 0.5)	-20.6 (± 0.5)
5805	37.4	113.6	(0.18-0''.72) (1.49-5.97 kpc)	-19.3 (± 0.4)	-19.3 (± 0.4)	-19.7 (± 0.4)	-19.3 (± 0.4)	-19.3 (± 0.4)
7556	36.9	175.3	(0.42-0''.90) (2.89-6.19 kpc)	18.9 (± 0.4)	19.7 (± 0.4)	21.2 (± 0.5)	22.2 (± 0.6)	24.7 (± 0.7)
8049	40.7	8.8	(0.36-1''.02) (2.01-5.69 kpc)	32.8 (± 1.1)	27.9 (± 0.9)	24.8 (± 0.7)	25.5 (± 0.7)	35.2 (± 1.3)
8585	36.0	24.0	(0.42-1''.02) (3.48-8.44 kpc)	-28.5 (± 0.9)	-26.8 (± 0.8)	-25.3 (± 0.7)	-26.1 (± 0.8)	-24.0 (± 0.7)
8810	33.0	117.8	(0.24-0''.72) (1.77-5.31 kpc)	--	--	17.7 (± 0.4)	18.4 (± 0.4)	19.2 (± 0.4)
9018	37.7	42.1	(0.24-0''.60) (1.99-4.96 kpc)	-35.0 (± 1.3)	-37.8 (± 1.5)	-37.8 (± 1.5)	-39.3 (± 1.6)	-53.2 (± 2.5)
9253	47.8	55.0	(0.60-1''.98) (4.26-14.05 kpc)	-78.7 (± 3.7)	-65.0 (± 3.1)	-53.7 (± 2.5)	-51.3 (± 2.3)	-49.1 (± 2.2)
9868	28.9	156.9	(1.08-1''.98) (8.95-16.41 kpc)	19.6 (± 0.4)	21.0 (± 0.5)	25.2 (± 0.7)	23.2 (± 0.6)	34.8 (± 1.3)

Table 5. Measured pitch angles (P) for the 60 mas data.

UDF-ID	F435W (°)	F606W (°)	F775W (°)	F814W (°)	F850LP (°)	F105W (°)	F125W (°)	F140W (°)	F160W (°)
656	-29.2 (± 1.0)	-25.6 (± 0.8)	-29.2 (± 1.0)	-33.8 (± 1.3)	-50.6 (± 2.6)	-48.1 (± 2.4)	-65.9 (± 3.6)	--	-77.4 (± 4.1)
2607	--	43.1 (± 2.0)	41.1 (± 1.9)	37.6 (± 1.6)	41.1 (± 1.9)	34.6 (± 1.4)	37.6 (± 1.6)	34.6 (± 1.4)	37.6 (± 1.6)
3180	--	-23.7 (± 0.7)	-27.9 (± 1.0)	-27.9 (± 1.0)	-27.9 (± 1.0)	-31.2 (± 1.2)	-32.4 (± 1.3)	-35.2 (± 1.5)	-35.2 (± 1.5)
3492	30.1 (± 1.0)	20.9 (± 0.5)	17.1 (± 0.3)	18.2 (± 0.4)	18.6 (± 0.4)	17.9 (± 0.4)	18.2 (± 0.4)	17.1 (± 0.3)	17.5 (± 0.4)
3822	--	16.5 (± 0.3)	18.0 (± 0.4)	19.3 (± 0.5)	23.1 (± 0.7)	26.8 (± 0.9)	27.7 (± 0.9)	26.8 (± 0.9)	33.0 (± 1.3)
4438	25.9 (± 0.8)	28.6 (± 1.0)	30.8 (± 1.2)	32.0 (± 1.2)	33.2 (± 1.3)	36.1 (± 1.5)	36.1 (± 1.5)	36.1 (± 1.5)	37.6 (± 1.6)
4929	--	-19.8 (± 0.5)	-19.8 (± 0.5)	-18.9 (± 0.5)	-18.9 (± 0.5)	-18.9 (± 0.5)	-18.4 (± 0.4)	--	--
5417	--	--	-21.3 (± 0.6)	-21.3 (± 0.6)	-21.3 (± 0.6)	-21.9 (± 0.6)	-22.5 (± 0.7)	-23.2 (± 0.7)	-23.2 (± 0.7)
5805	-21.4 (± 0.6)	-20.8 (± 0.6)	-20.8 (± 0.6)	-20.8 (± 0.6)	-20.3 (± 0.5)	-19.8 (± 0.5)	-20.8 (± 0.6)	--	--
7556	20.8 (± 0.6)	22.6 (± 0.7)	27.3 (± 0.9)	30.4 (± 1.1)	37.2 (± 1.6)	32.9 (± 1.3)	34.2 (± 1.4)	32.9 (± 1.3)	34.2 (± 1.4)
8049	41.0 (± 1.9)	31.8 (± 1.2)	26.6 (± 0.9)	27.5 (± 0.9)	52.5 (± 2.8)	49.8 (± 2.6)	65.3 (± 3.6)	69.0 (± 3.8)	72.9 (± 4.0)
8585	-32.8 (± 1.3)	-29.3 (± 1.1)	-27.3 (± 0.9)	-28.3 (± 1.0)	-25.5 (± 0.8)	-24.7 (± 0.8)	-23.3 (± 0.7)	-23.3 (± 0.7)	-22.0 (± 0.6)
8810	--	--	--	--	--	--	--	40.7 (± 1.9)	44.7 (± 2.2)
9018	-55.2 (± 3.0)	-55.2 (± 3.0)	-52.3 (± 2.8)	-52.3 (± 2.8)	-68.9 (± 3.9)	-55.2 (± 3.0)	-52.3 (± 2.8)	-55.2 (± 3.0)	-72.8 (± 4.0)
9253	--	-77.2 (± 4.1)	-58.8 (± 3.2)	-52.9 (± 2.8)	-41.4 (± 1.9)	-39.6 (± 1.8)	-32.2 (± 1.2)	-41.4 (± 1.9)	-32.2 (± 1.2)
9868	19.1 (± 0.5)	17.3 (± 0.4)	20.6 (± 0.6)	21.2 (± 0.6)	35.4 (± 1.5)	23.1 (± 0.7)	44.6 (± 2.2)	30.2 (± 1.1)	37.0 (± 1.6)

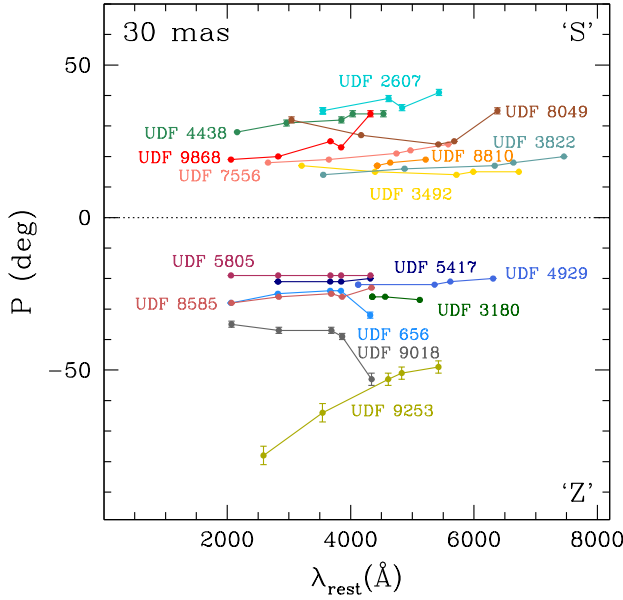


Figure 11. Measured pitch angles, P (deg), as a function of rest wavelength, λ_{rest} (Å), for the 30 mas XDF images in filters F435W, F606W, F775W, F814W, F850LP, and F105W. ‘S’ or ‘Z’ indicate the galaxies on-the-sky view.

4.2 Wavy patterns in the relation $|P|$ vs. λ_{rest}

In order to quantify the relation of $|P|$ with λ_{rest} we calculated linear fits to the NIR filters only. Although these fits represent a good approximation to the general trends, the distributions of all data points suggest that a higher degree polynomial may be better in certain cases. With this in mind, the relation of $|P|$ with λ_{rest} may be described as a ‘wavy’ pattern for some objects. In Figure 15 we show the most significant cases of ‘wavy’ patterns in our sample. Every fit (x , x^2 , x^3 and x^4) gives the same weight to all data points.

In the case of spirals with ‘normal’ colour jumps (see Table 6), the first aspect to notice is that the $|P|$ values at shorter wavelengths tend to switch, i.e., the $|P|$ value increases for shorter wavelengths. This may be explained if the classic age/colour gradients (see Figure 1, left panel) begins to dominate at places where the optical depth $\tau < 1$, although still close to the dust lane and to SF-arm. In other cases, P switches again at longer wavelengths. The pitch angle of the dust lanes, P_{shock} , can be smaller or equal to the pitch angle of the density wave traced by old stars, P_{pot} (Gittins & Clarke 2004). Thus, the wavy pattern may be explained as a combination of various factors, including dust lanes and colour jumps at longer λ_{rest} , as well as classic colour gradients at shorter wavelengths. However, the colour jump dominates most of the P measurements. This scenario may also explain the ‘reverse’ colour jumps discussed earlier. The ‘wavy’ pattern was also detected in the pitch angle measurements of spiral arms in galaxies at $z = 0$ by Yu & Ho (2018); 40% of their objects (see Figure 16) with optical, NUV and FUV data present this phenomenon. This con-

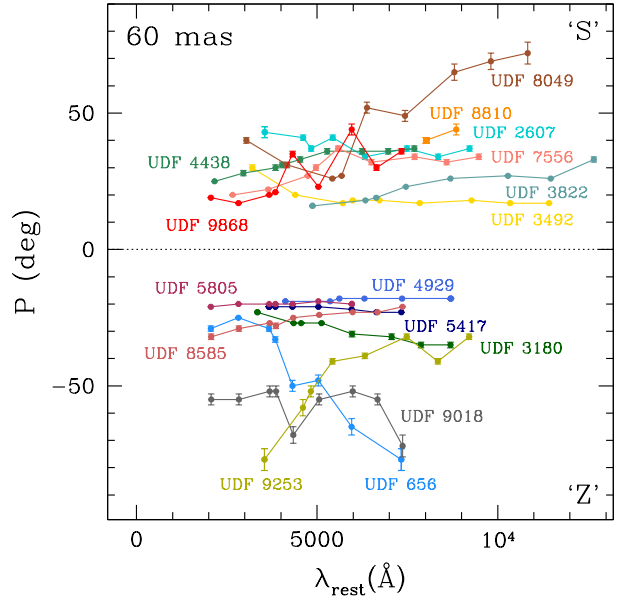


Figure 12. Same as Figure 11 for the 60 mas XDF images, in filters F435W, F606W, F775W, F814W, F850LP, F105W, F125W, F140W, and F160W.

clusion may also explain the findings of other authors for nearby galaxies (Pour-Imani et al. 2016; Miller et al. 2019; Abdeen et al. 2022), whose P measurements of the colour jump show smaller angles in the red than in the blue, as expected for the classic gradients. Unfortunately, the aforementioned works do not provide values for ΔR , and hence it is difficult to reproduce their results, and to compare them with those of other authors.

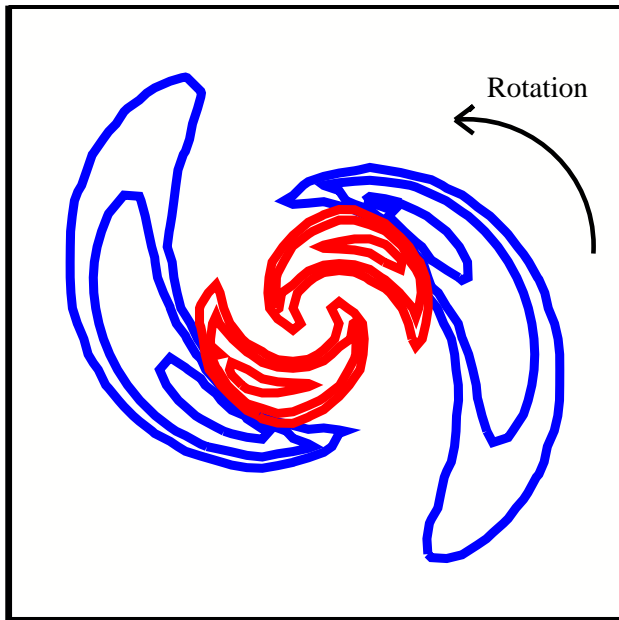
5 CONCLUSIONS

By measuring the pitch angles of distant galaxies in the Hubble XDF (Illingworth et al. 2013), we have found evidence of colour jumps (red-to-blue) across the spiral arms of disc galaxies at $z > 0$. Similarly to their local counterparts, most of these galaxies exhibit trailing spiral arms. However, for three out of sixteen objects the colour jump measurements are found to be reverse, i.e., blue-to-red, and may indicate leading spiral arms. Also, the behaviour of the pitch angle as a function of rest wavelength is not linear, but resembles a wavy pattern. We presume that the reverse colour jump and the wavy pattern may be due to a combination of classic age/colour gradients and colour jumps across the spiral arms, together with extinction due to the dust lanes.

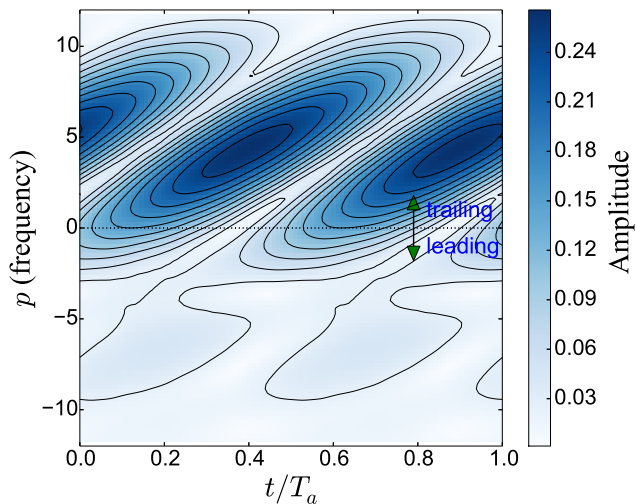
These results indicate that colour jumps can be observed across the spiral arms of galaxies between redshifts of $z = 0 - 1$, i.e., for the last ~ 8 Gyr. The onset of spiral structure may occur within the redshift range of $1.5 < z < 3$ (Elmegreen & Elmegreen 2014; Hodge et al. 2019; Margalef-Bentabol et al. 2022). Spiral galaxies at redshifts $z > 2$ may be common; for instance, we have

Table 6. Linear fits to the pitch angles, $P(\lambda_{\text{rest}}) = a + b\lambda_{\text{rest}}$, for filters F105W, F125W, F140W and F160W.

UDF-ID	View on the sky	a	b	r_{xy}	$\Delta\lambda_{\text{rest}}$ (Å)	Colour jump orientation
656	'Z'	11.86	-0.01239	-0.9724	(5033 - 7330)	normal
2607	'S'	30.81	0.00067	0.4743	(6330 - 9219)	normal
3180	'Z'	-21.24	-0.00166	-0.9461	(5970 - 8695)	normal
3492	'S'	15.79	0.00026	0.9992	(7841 - 9278)	normal
3822	'S'	14.51	0.00131	0.7418	(8694 - 12660)	normal
4438	'S'	32.75	0.00057	0.7410	(5282 - 7693)	normal
4929	'Z'	-21.33	0.00033	1.0000	(7351 - 8698)	reverse
5417	'Z'	-18.88	-0.00061	-0.9580	(5036 - 7334)	normal
5805	'Z'	-13.92	-0.00116	1.0000	(5036 - 5959)	normal
7556	'S'	31.19	0.00029	0.4743	(6506 - 9475)	normal
8049	'S'	2.67	0.00668	0.9569	(7435 - 10830)	normal
8585	'Z'	-30.23	0.00110	0.9580	(5055 - 7363)	reverse
8810	'S'	1.37	0.00490	1.0000	(8019 - 8851)	normal
9018	'Z'	-15.57	-0.00691	-0.7250	(5058 - 7367)	normal
9253	'Z'	-47.59	0.00143	0.3654	(6324 - 9211)	reverse
9868	'S'	8.08	0.00410	0.4387	(5037 - 7336)	normal

**Figure 13.** Contour plot of two rotating spiral patterns. The outer pattern (blue contours) has a pitch angle of $P = 24^\circ$, and the inner spiral (red contours) has $P = 27^\circ$.

the spiral galaxies HDFX 28 at $z = 2.011$ (Dawson et al. 2003), Q2343-BX442 at $z = 2.18$ (Law et al. 2012), A1689B11 at $z = 2.54$ (Yuan et al. 2017), A2744-DSG-z3 at $z = 3.059$ (Wu et al. 2022), and even BRI 1335-0417 at redshift 4.41 (Tsukui & Iguchi 2021). Besides, there is a predominance of disc galaxies for $z > 1.5$ (Ferreira et al. 2022; Robertson et al. 2022), and a growing evidence of cold rotating discs at $z > 4$ (e.g., De Breuck et al. 2014; Rizzo et al. 2020; Kretschmer, Dekel, & Teyssier 2022; Tokuoka et al. 2022). The results of this paper stress the importance of future studies with larger samples of distant disc galaxies in order to unveil the origin of spiral structure in the universe.

**Figure 14.** $A(m = 2, p)$ spectra resulting from the superposition of the two rotating spiral patterns shown in Figure 13, as a function of time, t . T_a represents the time needed for the inner pattern to complete one full revolution with respect to the outer pattern.

ACKNOWLEDGEMENTS

We acknowledge the reviewer for important comments and suggestions. EMG acknowledges support through the ‘Investigadores por México’ (formerly Cátedras CONACYT) program. RAGL acknowledges the financial support of CONACYT, Mexico, through project A1-S-8263.

DATA AVAILABILITY

Based on observations made with the NASA/ESA Hubble Space Telescope, <https://archive.stsci.edu/prepds/xd/>, and obtained from the Hubble Legacy Archive, <https://hla.stsci.edu/hlaview.html>; which is a collaboration between the Space Telescope Science Institute

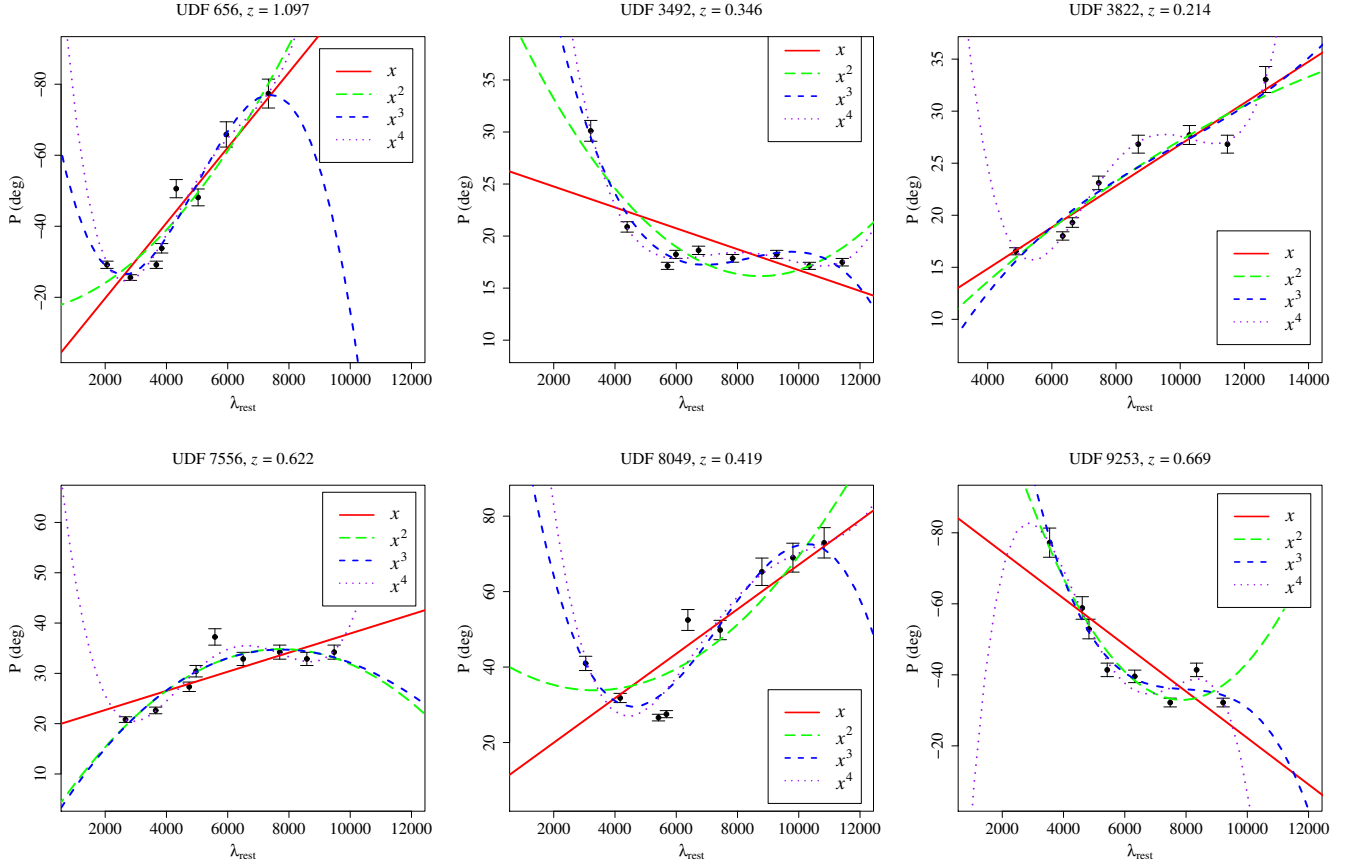


Figure 15. Polynomial fits to the pitch angle measurements, from the 60 mas data, of UDF 656, UDF 3492, UDF 3822, UDF 7556, UDF 8049, and UDF 9253. *Continuous red line:* linear x fit; *long-dashed green line:* second order x^2 fit; *short-dashed blue line:* third order x^3 fit; *dotted violet line:* fourth order x^4 fit. Notice the ‘wavy’ pattern of the data.

(STScI/NASA), the Space Telescope European Coordinating Facility (ST-ECF/ESA) and the Canadian Astronomy Data Centre (CADC/NRC/CSA).

Based on data obtained from the ESO Science Archive Facility, http://archive.eso.org/wdb/wdb/adp/phase3_spectral/form?collection_name=MUSE; under request numbers 647703, 647706, 647710, 647712, 647716, 647719, and 647724 ‘PHASE3’.

REFERENCES

- Abdeen S., Davis B. L., Eufrasio R., Kennefick D., Kennefick J., Miller R., Shields D., et al., 2022, MNRAS, 512, 366. doi:10.1093/mnras/stac459
- Adams D., Mehta V., Dickinson H., Scarlata C., Fortson L., Kruk S., Simmons B., et al., 2022, ApJ, 931, 16. doi:10.3847/1538-4357/ac6512
- Ahn C. P., Alexandroff R., Allende Prieto C., Anders F., Anderson S. F., Anderton T., Andrews B. H., et al., 2014, ApJS, 211, 17. doi:10.1088/0067-0049/211/2/17
- Alam S., Albareti F. D., Allende Prieto C., Anders F., Anderson S. F., Anderton T., Andrews B. H., et al., 2015, ApJS, 219, 12. doi:10.1088/0067-0049/219/1/12
- Aniano G., Draine B. T., Gordon K. D., Sandstrom K., 2011, PASP, 123, 1218. doi:10.1086/662219
- Athanassoula E., 2012, MNRAS, 426, L46. doi:10.1111/j.1745-3933.2012.01320.x
- Bacon R., Accardo M., Adjali L., Anwand H., Bauer S., Biswas I., Blaizot J., et al., 2010, SPIE, 7735, 773508. doi:10.1117/12.856027
- Bacon R., Conseil S., Mary D., Brinchmann J., Shepherd M., Akhlaghi M., Weilbacher P. M., et al., 2017, A&A, 608, A1. doi:10.1051/0004-6361/201730833
- Bacon R., Mary D., Garel T., Blaizot J., Maseda M., Schaye J., Wisotzki L., et al., 2021, A&A, 647, A107. doi:10.1051/0004-6361/202039887
- Beckwith S. V. W., Stiavelli M., Koekemoer A. M., Caldwell J. A. R., Ferguson H. C., Hook R., Lucas R. A., et al., 2006, AJ, 132, 1729. doi:10.1086/507302
- Bertin G., Lin C. C., Lowe S. A., Thurstans R. P., 1989, ApJ, 338, 78. doi:10.1086/167182
- Benítez N., 2000, ApJ, 536, 571. doi:10.1086/308947
- Bennett C. L., Larson D., Weiland J. L., Hinshaw G., 2014, ApJ, 794, 135. doi:10.1088/0004-637X/794/2/135
- Bevington, P. R. 1969, Data reduction and error analysis for the physical sciences, New York: McGraw-Hill
- Block D. L., Puerari I., Takamiya M., Abraham R., Stockton A., Robson I., Holland W., 2001, A&A, 371, 393. doi:10.1051/0004-6361:20010081
- Boquien M., Burgarella D., Roehlly Y., Buat V., Ciesla L., Corre D., Inoue A. K., et al., 2019, A&A, 622, A103. doi:10.1051/0004-6361/201834156

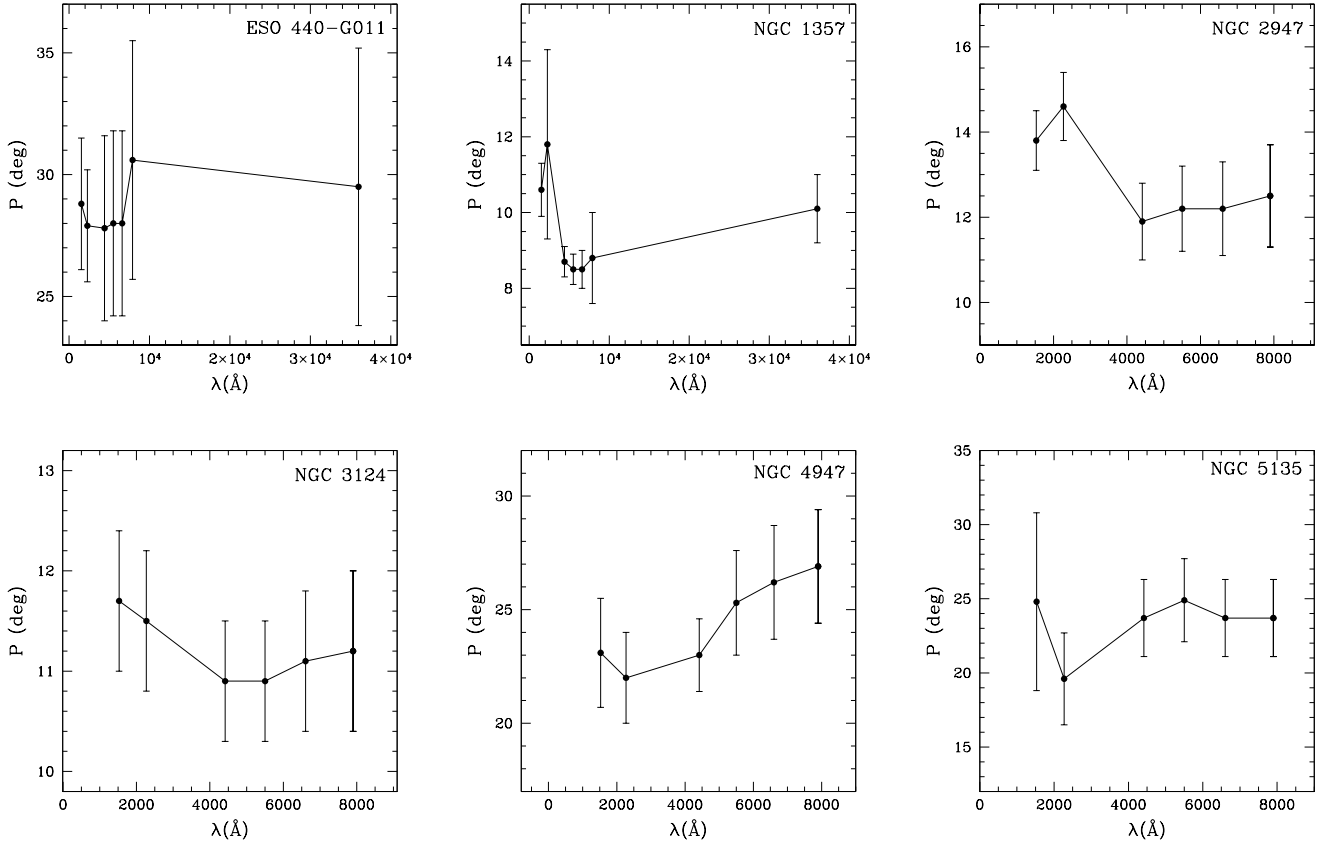


Figure 16. Examples of ‘wavy’ patterns detected in the P measurements of ESO 440-GO11, NGC 1357, 2947, 3124, 4947, and NGC 5135, performed by Yu & Ho (2018).

- Burgarella D., Buat V., Iglesias-Páramo J., 2005, MNRAS, 360, 1413. doi:10.1111/j.1365-2966.2005.09131.x
- Calvi V., Stiavelli M., Bradley L., Pizzella A., Kim S., 2014, ApJ, 796, 102. doi:10.1088/0004-637X/796/2/102
- Cedrés B., Cepa J., Bongiovanni Á., Castañeda H., Sánchez-Portal M., Tomita A., 2013, A&A, 560, A59. doi:10.1051/0004-6361/201321588
- Coe D., Benítez N., Sánchez S. F., Jee M., Bouwens R., Ford H., 2006, AJ, 132, 926. doi:10.1086/505530
- Contopoulos G., 2022, arXiv, arXiv:2210.13632
- Dawson S., McCrady N., Stern D., Eckart M. E., Spinrad H., Liu M. C., Graham J. R., 2003, AJ, 125, 1236. doi:10.1086/367792
- De Breuck C., Williams R. J., Swinbank M., Caselli P., Coppin K., Davis T. A., Maiolino R., et al., 2014, A&A, 565, A59. doi:10.1051/0004-6361/201323331
- Dobbs C., Baba J., 2014, PASA, 31, e035. doi:10.1017/pasa.2014.31
- Egusa F., Sofue Y., Nakanishi H., 2004, PASJ, 56, L45. doi:10.1093/pasj/56.6.L45
- Egusa F., Kohno K., Sofue Y., Nakanishi H., Komugi S., 2009, ApJ, 697, 1870. doi:10.1088/0004-637X/697/2/1870
- Elmegreen B. G., Elmegreen D. M., Seiden P. E., 1989, ApJ, 343, 602. doi:10.1086/167733
- Elmegreen B. G., 1995, in: Ferrara A., McKee C.F., Helles C., Shapiro P.R. (eds.), Physics of the Interstellar Medium and Intergalactic Medium, ASP Conference Series, 80, p. 218
- Elmegreen D. M., Elmegreen B. G., 2014, ApJ, 781, 11. doi:10.1088/0004-637X/781/1/11
- Ferreira L., Adams N., Conselice C. J., Sazonova E., Austin D., Caruana J., Ferrari F., et al., 2022, arXiv, arXiv:2207.09428
- Gerola H., Seiden P. E., 1978, ApJ, 223, 129. doi:10.1086/156243
- Gil de Paz A., Boissier S., Madore B. F., Seibert M., Joe Y. H., Boselli A., Wyder T. K., et al., 2007, ApJS, 173, 185. doi:10.1086/516636
- Gittins D. M., Clarke C. J., 2004, MNRAS, 349, 909. doi:10.1111/j.1365-2966.2004.07560.x
- Goldreich P., Tremaine S., 1978, ApJ, 222, 850. doi:10.1086/156203
- Gonzalez R. A., Graham J. R., 1996, ApJ, 460, 651. doi:10.1086/176999
- Grand R. J. J., Kawata D., Cropper M., 2013, A&A, 553, A77. doi:10.1051/0004-6361/201321308
- Grogan N. A., Kocevski D. D., Faber S. M., Ferguson H. C., Koekemoer A. M., Riess A. G., Acquaviva V., et al., 2011, ApJS, 197, 35. doi:10.1088/0067-0049/197/2/35
- Grosbøl P., 1988, in: Benney D., Shu F., Yuan C. (eds.), Applied Mathematics, Fluid Mechanics, and Astrophysics: A Symposium to Honour C.C. Lin. Singapore World Scientific Publishing Co., p. 345
- Grosbøl P. J., Patsis P. A., 1998, A&A, 336, 840
- Grosbøl P. J., Block D. L., Patsis P. A., 1999, Ap&SS, 269, 423. doi:10.1023/A:1017073719292
- Grosbøl P., Dottori H., 2009, A&A, 499, L21. doi:10.1051/0004-6361/200911805
- Grouchy R. D., Buta R., Salo H., Laurikainen E., Speltincx T., 2008, AJ, 136, 980. doi:10.1088/0004-6256/136/3/980

- Hodge J. A., Smail I., Walter F., da Cunha E., Swinbank A. M., Rybak M., Venemans B., et al., 2019, ApJ, 876, 130. doi:10.3847/1538-4357/ab184

Illingworth G. D., Magee D., Oesch P. A., Bouwens R. J., Labb   I., Stiavelli M., van Dokkum P. G., et al., 2013, ApJS, 209, 6. doi:10.1088/0067-0049/209/1/6

Inami H., Bacon R., Brinchmann J., Richard J., Contini T., Conseil S., Hamer S., et al., 2017, A&A, 608, A2. doi:10.1051/0004-6361/201731195

Karapetyan A. G., 2022, MNRAS, 517, L132. doi:10.1093/mnrasl/slac121

Kretschmer M., Dekel A., Teyssier R., 2022, MNRAS, 510, 3266. doi:10.1093/mnras/stab3648

La Vigne M. A., Vogel S. N., Ostriker E. C., 2006, ApJ, 650, 818. doi:10.1086/506589

Law D. R., Shapley A. E., Steidel C. C., Reddy N. A., Christensen C. R., Erb D. K., 2012, Natur, 487, 338. doi:10.1038/nature11256

Leroy A. K., Walter F., Brinks E., Bigiel F., de Blok W. J. G., Madore B., Thornley M. D., 2008, AJ, 136, 2782. doi:10.1088/0004-6256/136/6/2782

Lieb E., Collier A., Madigan A.-M., 2022, MNRAS, 509, 685. doi:10.1093/mnras/stab2904

Lin C. C., Shu F. H., 1964, ApJ, 140, 646. doi:10.1086/147955

Lin Z., Xu Y., Hou L., Liu D., Li Y., Hao C., Li J., et al., 2022, ApJ, 931, 72. doi:10.3847/1538-4357/ac67a6

Lorenz B., Kriek M., Shapley A. E., Reddy N. A., Sanders R. L., Barro G., Coil A. L., et al., 2023, arXiv, arXiv:2304.08521

Margalef-Bentabol B., Conselice C. J., Haeussler B., Casteels K., Lintott C., Masters K., Simmons B., 2022, MNRAS, 511, 1502. doi:10.1093/mnras/stac080

Mark J. W. K., 1976, ApJ, 205, 363. doi:10.1086/154287

Mart  nez-Garc  a E. E., Gonz  lez-L  pezlira R. A., Bruzual-A. G., 2009, ApJ, 694, 512. doi:10.1088/0004-637X/694/4/512

Mart  nez-Garc  a E. E., Gonz  lez-L  pezlira R. A., G  mez G. C., 2009, ApJ, 707, 1650. doi:10.1088/0004-637X/707/2/1650

Mart  nez-Garc  a E. E., Gonz  lez-L  pezlira R. A., 2011, ApJ, 734, 122. doi:10.1088/0004-637X/734/2/122

Mart  nez-Garc  a E. E., Gonz  lez-L  pezlira R. A., 2013, ApJ, 765, 105. doi:10.1088/0004-637X/765/2/105

Mart  nez-Garc  a E. E., Puerari I., 2014, ApJ, 790, 118. doi:10.1088/0004-637X/790/2/118

Mart  nez-Garc  a E. E., Puerari I., Rosales-Ortega F. F., Gonz  lez-L  pezlira R. A., Fuentes-Carrera I., Luna A., 2014, ApJL, 793, L19. doi:10.1088/2041-8205/793/1/L19

Mart  nez-Garc  a E. E., 2012, ApJ, 744, 92. doi:10.1088/0004-637X/744/2/92

Mart  nez-Garc  a E. E., Gonz  lez-L  pezlira R. A., 2015, HiA, 16, 323. doi:10.1017/S1743921314005870

McQuinn K. B. W., Skillman E. D., Dolphin A. E., Berg D., Kennicutt R., 2016, ApJ, 826, 21. doi:10.3847/0004-637X/826/1/21

Melia F., Yennapureddy M. K., 2018, MNRAS, 480, 2144. doi:10.1093/mnras/sty1962

Michikoshi S., Kokubo E., 2014, ApJ, 787, 174. doi:10.1088/0004-637X/787/2/174

Miller R., Kennefick D., Kennefick J., Shameer Abdeen M., Monson E., Eufrasio R. T., Shields D. W., et al., 2019, ApJ, 874, 177. doi:10.3847/1538-4357/ab0d26

Mueller M. W., Arnett W. D., 1976, ApJ, 210, 670. doi:10.1086/154873

Noll S., Burgarella D., Giovannoli E., Buat V., Marcillac D., Mu  oz-Mateos J. C., 2009, A&A, 507, 1793. doi:10.1051/0004-6361/200912497

Patsis P. A., 2006, MNRAS, 369, L56. doi:10.1111/j.1745-3933.2006.00174.x

Peterken T. G., Merrifield M. R., Arag  n-Salamanca A., Drory N., Krawczyk C. M., Masters K. L., Weijmans A.-M., et al., 2019, NatAs, 3, 178. doi:10.1038/s41550-018-0627-5

Pour-Imani H., Kennefick D., Kennefick J., Davis B. L., Shields D. W., Shameer Abdeen M., 2016, ApJL, 827, L2. doi:10.3847/2041-8205/827/1/L2

Puerari I., Elmegreen B. G., Block D. L., 2014, AJ, 148, 133. doi:10.1088/0004-6256/148/6/133

Puerari I., Block D. L., Elmegreen B. G., Frogel J. A., Eskridge P. B., 2000, A&A, 359, 932

Puerari I., Dottori H. A., 1992, A&AS, 93, 469

Puerari I., Dottori H., 1997, ApJL, 476, L73. doi:10.1086/310502

Rafelski M., Teplitz H. I., Gardner J. P., Coe D., Bond N. A., Koekemoer A. M., Grogan N., et al., 2015, AJ, 150, 31. doi:10.1088/0004-6256/150/1/31

Rizzo F., Vegetti S., Powell D., Fraternali F., McKean J. P., Stacey H. R., White S. D. M., 2020, Natur, 584, 201. doi:10.1038/s41586-020-2572-6

Roberts W. W., 1969, ApJ, 158, 123. doi:10.1086/150177

Robertson B. E., Tacchella S., Johnson B. D., Hausen R., Alabi A. B., Boyett K., Bunker A. J., et al., 2022, arXiv, arXiv:2208.11456

Romero-G  mez M., Masdemont J. J., Athanassoula E., Garc  a-G  mez C., 2006, A&A, 453, 39. doi:10.1051/0004-6361:20054653

S  nchez-Gil M. C., Jones D. H., P  rez E., Bland-Hawthorn J., Alfaro E. J., O'Byrne J., 2011, MNRAS, 415, 753. doi:10.1111/j.1365-2966.2011.18759.x

Saraiva Schroeder M. F., Pastoriza M. G., Kepler S. O., Puerari I., 1994, A&AS, 108, 41

Sattari Z., Mobasher B., Chartab N., Kelson D. D., Teplitz H. I., Rafelski M., Grogan N. A., et al., 2023, arXiv, arXiv:2305.09021. doi:10.48550/arXiv.2305.09021

Sellwood J. A., Carlberg R. G., 1984, ApJ, 282, 61. doi:10.1086/162176

Sellwood J. A., Carlberg R. G., 2014, ApJ, 785, 137. doi:10.1088/0004-637X/785/2/137

Sellwood J. A., Carlberg R. G., 2021, MNRAS, 500, 5043. doi:10.1093/mnras/staa3499

Sellwood J. A., Trick W. H., Carlberg R. G., Coronado J., Rix H.-W., 2019, MNRAS, 484, 3154. doi:10.1093/mnras/stz140

Sellwood J. A., Masters K. L., 2022, ARA&A, 60, arXiv:2110.05615

Shaver P. A., Wall J. V., Kellermann K. I., Jackson C. A., Hawkins M. R. S., 1996, Natur, 384, 439. doi:10.1038/384439a0

Shetty R., Ostriker E. C., 2006, ApJ, 647, 997. doi:10.1086/505594

Shu F. H., 2016, ARA&A, 54, 667. doi:10.1146/annurev-astro-081915-023426

Tamburro D., Rix H.-W., Walter F., Brinks E., de Blok W. J. G., Kennicutt R. C., Mac Low M.-M., 2008, AJ, 136, 2872. doi:10.1088/0004-6256/136/6/2872

Tokuoka T., Inoue A. K., Hashimoto T., Ellis R. S., Laporte N., Sugahara Y., Matsuo H., et al., 2022, arXiv, arXiv:2205.14378

Toomre A., 1981, in: The structure and evolution of normal galaxies, ed. S.M. Fall, & D. Lynden-Bell. Cambridge and New York, Cambridge University Press, 111

Tsukui T., Iguchi S., 2021, Sci, 372, 1201. doi:10.1126/science.abe9680

V  ais  nen P., Ryder S., Mattila S., Kotilainen J., 2008, ApJL, 689, L37. doi:10.1086/595728

Valencia-Enr  quez D., Puerari I., Chaves-Velasquez L., 2017, RMxAA, 53, 257

Vall  e J. P., 2021, MNRAS, 506, 523. doi:10.1093/mnras/stab1679

Vall  e J. P., 2021, IJAA, 11, 445. doi:10.4236/ijaa.2021.114022

Windhorst R. A., Cohen S. H., Hathi N. P., McCarthy P. J., Ryan R. E., Yan H., Baldry I. K., et al., 2011, ApJS, 193, 27. doi:10.1088/0067-0049/193/2/27

Wright E. L., 2006, PASP, 118, 1711. doi:10.1086/510102

- Wu Y., Cai Z., Sun F., Bian F., Lin X., Li Z., Li M., et al., 2022,
arXiv, arXiv:2208.08473
- Yuan T., Richard J., Gupta A., Federrath C., Sharma S.,
Groves B. A., Kewley L. J., et al., 2017, ApJ, 850, 61.
doi:10.3847/1538-4357/aa951d
- Yu S.-Y., Ho L. C., 2018, ApJ, 869, 29. doi:10.3847/1538-
4357/aaeacd
- Zibetti S., Charlot S., Rix H.-W., 2009, MNRAS, 400, 1181.
doi:10.1111/j.1365-2966.2009.15528.x

APPENDIX A: CONFIGURATION USED IN CIGALE

In this section we list the input parameters configuration used in **CIGALE** (cf. Boquien et al. 2019) to fit the HUDF galaxies with Rafelski et al. (2015) photometry.

- **sfh2exp** module
 - tau_main = 1000, 2000, 3000, 5000, 7000 (Myr)
 - tau_burst = 10, 20, 30, 50, 70 (Myr)
 - f_burst = 0.01, 0.1, 0.2, 0.4, 0.6
 - age = 3000, 5000, 7000, 9000, 11000, 13000 (Myr)
 - burst_age = 200, 600, 800, 1000 (Myr)
 - sfr_0 = 1.0 ($M_{\odot} \text{ yr}^{-1}$)
 - normalise = True
- **bc03** module
 - imf = 1 (Chabrier)
 - metallicity = 0.0001, 0.0004, 0.004, 0.008, 0.02, 0.05
 - separation_age = 10 (Myr)
- **dustatt_modified_CF00** module
 - Av_ISM = 1, 2, 3 ,4
 - mu = 0.1, 0.3, 0.6, 0.9
 - slope_ISM = -0.7
 - slope_BC = -1.3

With this configuration **CIGALE** computes 4.32×10^6 models, i.e., every combination of the input parameters.

This paper has been typeset from a TeX/LaTeX file prepared by the author.